

Department of Physics and Astronomy
Experimental Particle Physics Group
Kelvin Building, University of Glasgow
Glasgow, G12 8QQ, Scotland
Telephone: +44 (0)141 330 2000 Fax: +44 (0)141 330 5881

**Synchrotron tests of 3D Medipix2 and TimePix
X-Ray Detectors**

Aaron Mac Raighne^{a*}, K. C. Akiba^h, L. Alianelli^b, M. Artuso^j, R. Bates^a, F. Bayer, J. Buytaert^c, P. Collins^d, M. Crossley^e, L. Eklund^a, C. Fleta^c, A. Gallas^e, M. Gandelmanⁱ, M. Gersabeck^a, E.N. Gimenez^b, V. Gligorov^a, T. Huse^f, M. John^g, L. F. Llin^a, M. Lozano^c, D. Maneuski^a, J. Marchal^b, T. Michel^k, M. Nicol^a, G. Pellegrini^c, D. E. Perira^e, R. Plackett^d, V. O'Shea^a, C. Parkes^a, E. Rodrigues^a, K.J.S. Sawhney^b, N. Tartoni^b, P. Vazquez^c

^a Department of Physics and Astronomy, University of Glasgow, Scotland, UK.

^b Diamond Light Source Ltd, Oxfordshire, UK.

^c Instituto de Microelectronica de Barcelona, Barcelona, Spain.

^d CERN CH-1211, Genève 23, Switzerland.

^e Facultad de Fisica , University of Santiago de Compostela, Spain.

^f Dept. of Physics, The University of Liverpool, Liverpool, U.K.

^g Dept. of Physics, University of Oxford, UK.

^h Nikhef, Science Park 105, 1098 XG Amsterdam, The Netherlands.

ⁱ Instituto de Fisica, Univ. Federal do Rio de Janeiro, Brazil.

^j Syracuse University, Syracuse, NY 13244, U.S.A.

^k Erlangen Centre for Astroparticle Physics, Universität Erlangen-Nürnberg, Erwin-Rommel-Str. 1,
91058 Erlangen, Germany

* Email: a.macraighne@physics.gla.ac.uk

Abstract

In this article we report on the use micro-focus synchrotron X-ray radiation and pion beams to compare the detection efficiencies and charge sharing properties of novel 3D detectors to that of the current planar technology. Detector substrates are bump-bonded to the Medipix2 and Timepix chips. 55µm square pixel maps of the detection efficiencies have been produced using X-ray and MIP beams. For X-rays, a drop of 3-4% detection efficiency over the pixel area was found due to the central electrode. The corner electrodes show no degradation in efficiency compared to that of the planar device. For MIPs a drop of 0.5% in efficiency due to the central electrode was observed. Evidence of a considerable reduction in charge sharing in the 3D detectors compared to the planar devices is also shown.

Synchrotron tests of 3D Medipix2 and TimePix X-Ray Detectors

Aaron Mac Raighne^a, K. C. Akiba^h, L. Alianelli^b, M. Artuso^j, R. Bates^a, F. Bayer, J. Buytaert^e, P. Collins^d, M. Crossley^e, L. Eklund^a, C. Fleta^c, A. Gallas^e, M. Gandelmanⁱ, M. Gersabeck^a, E.N. Gimenez^b, V. Gligorov^a, T. Huse^f, M. John^g, L. F. Llin^a, M. Lozano^c, D. Maneuski^a, J. Marchal^b, T. Michel^k, M. Nicol^a, G. Pellegrini^c, D. E. Perira^e, R. Plackett^d, V. O'Shea^a, C. Parkes^a, E. Rodrigues^a, K.J.S. Sawhney^b, N. Tartoni^b, P. Vazquez^e

Abstract – In this article we report on the use micro-focus synchrotron X-ray radiation and pion beams to compare the detection efficiencies and charge sharing properties of novel 3D detectors to that of the current planar technology. Detector substrates are bump-bonded to the Medipix2 and Timepix chips. 55 μm square pixel maps of the detection efficiencies have been produced using X-ray and MIP beams. For X-rays, a drop of 3-4% detection efficiency over the pixel area was found due to the central electrode. The corner electrodes show no degradation in efficiency compared to that of the planar device. For MIPs a drop of 0.5% in efficiency due to the central electrode was observed. Evidence of a considerable reduction in charge sharing in the 3D detectors compared to the planar devices is also shown.

I. INTRODUCTION

Current and planned synchrotron experiments require fast, high resolution, large area, efficient and radiation hard detectors [1]. Planar silicon detectors have found applications in this area but suffer from some limitations. 3D detectors offer advantages over the planar structures in many of the aforementioned areas. Faster, larger area, higher resolution and more radiation-hard detectors are possible with a 3D structure balanced against the decrease in the detection efficiency due to the electrode structure.

A. Double Sided 3D detectors

Double sided 3D detectors are variations of previous 3D designs where the electrode columns pass through the entire detector substrate [2]. They are designed to simplify the fabrication process and also to give more mechanical stability to the detector [3], [4]. The columns of one doping type are etched from the front surface and individually connected to readout electronics. The other columns are etched from the back surface and used to bias the detector. These 3D sensors were designed by Glasgow and CNM and fabricated by IMB-

CNM on a 285 μm substrate. Columns were 10 μm wide and 250 μm long. Schematics of the planar detector and the 3D detector are shown in Figure 1. Shown is a 3D N-type detector which is a hole collecting device. Also fabricated was an electron collecting device, named a 3D P-type detector, with a Si-P substrate and an N-doped column connected to the electronic read-out.

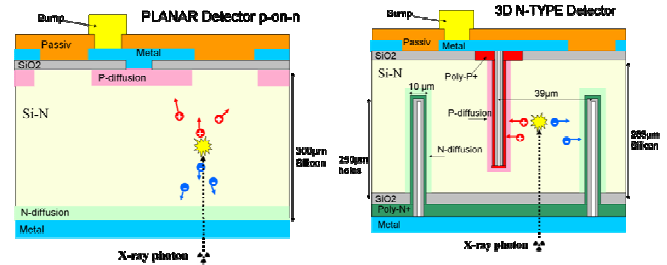


Fig. 1. Schematics of the planar and 3D detectors.

It is evident from the schematics in Figure 1 that the electrode separation in the planar device is defined by the substrate thickness which is of the order of 300 μm . In the 3D devices the electrode separation is reduced to $\sim 40\mu\text{m}$. This reduces the charge collection time, therefore faster devices are possible. With a reduction in charge collection time there are fewer opportunities for charge trapping to occur in irradiated devices (this is shown in a paper by R. Bates *et al.* in these proceedings). For large area detectors the 3D structure has advantages for the creation of tiled detectors. The need for guard rings can be removed and the dead area between separate detector devices can be reduced.

To create higher resolution detectors charge-sharing between pixels must be reduced. Charge clouds created by incident radiation will drift in the electric field parallel to the pixel boundaries. As the charge drifts lateral diffusion will cause the cloud to expand. This leads to neighbouring pixels collecting some of the incident charge and a blurring of the image. In the 3D configuration the charge cloud is pulled away from the pixel boundary, thus reducing the charge sharing [5].

B. Medipix2 and Timepix Read-out ASICs

Medipix2 and Timepix chips are read-out ASICs produced by the Medipix collaboration for hybrid pixel detectors. The Medipix2 detectors are 256*256 pixel detectors with 55 μm square pixels. Each pixel contains a preamplifier which can be programmed to collect holes or electrons, which allows all our

a) University of Glasgow, Dept. of Physics & Astronomy, Glasgow, UK.

b) Diamond Light Source Ltd, Oxfordshire, UK.

c) Instituto de Microelectronica de Barcelona, Barcelona, Spain.

d) CERN CH-1211, Genève 23, Switzerland.

e) Facultad de Fisica, University of Santiago de Compostela, Spain.

f) Dept. of Physics, The University of Liverpool, Liverpool, U.K.

g) Dept. of Physics, University of Oxford, UK.

h) Nikhef, Science Park 105, 1098 XG Amsterdam, The Netherlands.

i) Instituto de Fisica, Univ. Federal do Rio de Janeiro, Brazil.

j) Syracuse University, Syracuse, NY 13244, U.S.A.

k) Erlangen Centre for Astroparticle Physics, Universität Erlangen-Nürnberg, Erwin-Rommel-Str. 1, 91058 Erlangen, Germany

planar, N-type and P-type 3D devices to be bonded to the same type chip. Two thresholds levels are available to create an energy window, although in this report only a lower energy discriminator was used. Threshold levels can be set globally across the pixel matrix but each pixel contains 3-bit fine-tuning for threshold equalisation across the matrix. During acquisition each pixel has a 13-bit counter which provides the high dynamic range of the detector. When in readout mode these counters can be connected and the entire chip can be read-out in $300\mu\text{s}$ [6].

In addition to these traits the Timepix chip can resolve the energy of the incident radiation. In Time-Over-Threshold (TOT) mode the pixel counter remains counting while the input charge is above threshold. The counts present in each pixel give the energy of the charge cloud created in the detector pixel [7].

II. X-RAY BEAM

A. Experimental Set-up

The experimental set-up used was the B16 beamline at the Diamond Light Source, synchrotron research facility. The beamline comprises of a water-cooled fixed-exit double crystal monochromator that is capable of providing monochromatic beams over 2-20 keV photon energy. Downstream of the monochromator is a Toroidal mirror that normally focuses the X-ray beam with 1:1 magnification at 44 m of the source. For the measurements reported here, however, the mirror was retracted from the beam path to allow in the unfocused monochromatic beam to the experiments hutch (EH). X-rays of energy 14.5 keV were used to derive a micro-focused beam, using a compound refractive lens (CRL). The CRL was comprised of 27 lenses stacked in line in a He-filled chamber. All the lenses were identical: made of beryllium, of parabolic shape, with a radius of 0.2mm at the apex and a geometrical aperture of 1mm. The parabolic shape provides 2 dimensional focusing. The CRL lens chamber was installed on a 5-axis diffractometer in the EH, and was aligned in to the synchrotron beam using the fine angular and linear motions available on the diffractometer. This was achieved by observing the image on an area detector that had an effective pixel size of $6.5\mu\text{m}$. The Medipix detector was installed *ca.* 2.4m downstream of these lenses, on a versatile optics table. As the source was 44m upstream of the diffractometer this geometry provided *ca.* 18-fold demagnification. Size of the micro-focused beam was measured by doing transmission scans of $200\mu\text{m}$ diameter Au cross-wires. The derivatives of the wire scans gave the beam size. Beam size FWHM $4.5\pm 0.3\mu\text{m}$ in vertical and $6.7\pm 0.3\mu\text{m}$ in horizontal direction were measured. The beam size remained constant, within the error limits, over the days of detector characterization, as verified by beam size measurements done before and after the experiments. The devices under test were then placed at the focal plane on a stage with six degrees of freedom, Figure 2. The USB interface [8] and Pixelman software produced by IEAP was used to connect and control the chip. The translation stages had $0.1\mu\text{m}$ precision and $5\mu\text{rad}$ accuracy was available on the rotational stages. A high level of accuracy was required to

position the detector surface perpendicular to the beam. The alignment procedure was as follows.

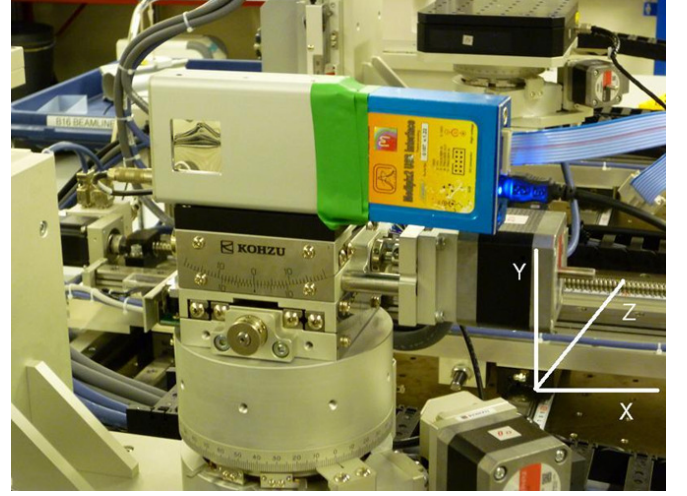


Fig. 2. Detector in its housing box with readout card, mounted on the motorized stage. The co-ordinate system is indicated. The stage rotation mechanism about the Y-axis and Z-axis is clearly visible.

The detector was positioned approximately perpendicular to the beam and rotated by β degrees (typically 45°) around the Y-axis. The pixel registering the peak intensity of counts from the beam was then located on the detector. The detector was moved a known distance along X using the automated stage where the peak intensity pixel was again recorded. The distance between the two beam positions on the detector is D1, see Figure 3.

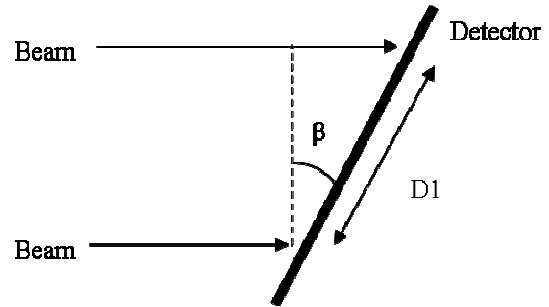


Fig. 3. Illustration of alignment procedure. The detector was rotated by angle β and the two beam central positions are measured as a distance D1 apart on the detector.

The detector was then rotated in the opposite direction by the same angle ($-\beta$) from the nominal perpendicular position and the process repeated to determine a distance between the two illuminated pixels, D2. If the detector is well aligned D1 and D2 should be equal, if not a correction angle can be derived using the following equation

$$\tan \theta \tan \beta = \frac{D1 - D2}{D1 + D2}, \quad (1)$$

where θ is the correction angle. Having applied the correction the process was repeated and any iteration of the procedure necessary was completed until the correction angle was minimised to 0 degrees within error.

Having preformed the alignment around the Y axis, the process was repeated for the alignment for the X axis. The rotation angle around the X axis was limited by the stage and a β of 10° was typically used.

The alignment measurements in both axes were repeated at the end of the data taking of each detector to check that the detector had not moved during the measurements.

The accuracy of the alignment was estimated by two methods. Eight repeated measurements of the alignment were made using the method discussed above for one detector and the rms calculated. The uncertainty on the alignment was calculated by error propagation due to the uncertainty arising from mis-measuring the beam position by one pixel. The error in the position of the stage was negligible. The results from both methods were in excellent agreement.

An alignment accuracy of 0.3 degrees on rotations about the Y-axis and 0.9 degrees on rotations about the X-axis were achieved. This alignment accuracy corresponds to a deviation of 2 to $5\mu\text{m}$ from a perpendicular line through the detector substrate. This can be compared with the nominal diameter of a pore in the 3D detector of $10\mu\text{m}$ as a measure of the alignment scale required.

With the position of the detector surface set perpendicular to the beam preliminary scans were preformed to estimate the sub-pixel position on the pixel matrix. The beam was set close to a corner of a pixel and a scan of a square area of $77.5\mu\text{m}$ was preformed in $2.5\mu\text{m}$ steps. This was done to ensure an entire pixel area was scanned in all cases.

At each scan position the values of the central pixel and its neighbours were added together to give the sum of a 3×3 pixel array. A 2D map of summed values was created using the beam position. The resulting distribution characterises the response of the pixels, Figure 4.

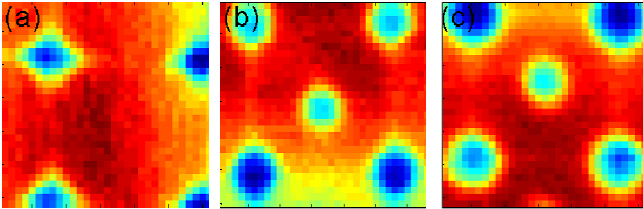


Fig. 4. $77.5\mu\text{m}$ square pixel maps of the three detectors investigated (a) Planar, (b) P-type, (c) N-type.

B. Background Subtraction

It was noticed that when our micro-focus beam was in the central region of the central pixel counts were found the surrounding pixels. This could not be due to charge sharing and must be due to a background signal, possibly caused by a factor in the focussing of the X-ray beam. To map this background a number of acquisitions were the micro-focus beam was in the central region of the central pixel were analysed. There should be no charge sharing effects on the neighbours in these acquisitions. A map was built up using the values from a pixel region surrounding the central pixel. The pixel values were separated on the map by their pixel position, steps of $55\mu\text{m}$, and their scan position, steps of $2.5\mu\text{m}$. The

map is shown in Figure 5(a). It can be seen that the signal is dominated by the central pixel which contains the highly focussed beam. With the central pixel removed a surface fit of the background in the neighbouring pixels is shown in Figure 5(b).

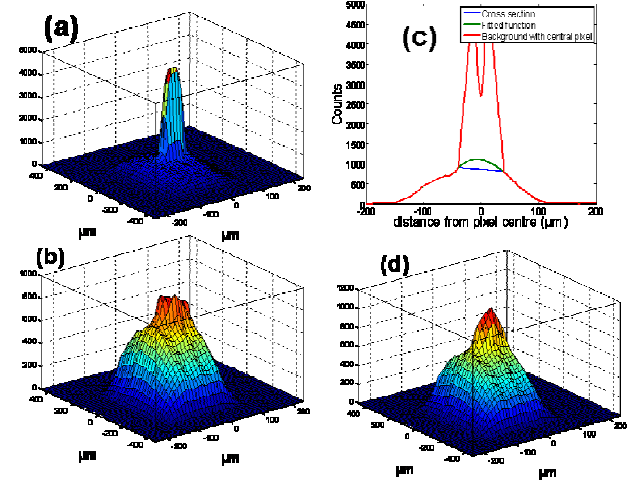


Fig. 5. Figure showing background estimation method; (a) Surface fit of the background and the signal in the central pixel due to micro-focus beam; (b) Background from neighbouring pixels with interpolation across the central pixel; (c) plot showing the cross sections of the full built up image, that of the background without the central pixel and that with the smoothing spline; and (d) Surface fit to estimated background.

To estimate the background in the central pixel, line sections of the surface fit are taken in X and Y and smoothing splines fitted, an example of which is shown in Figure 5(c). The line sections are added to the surface fit to give the estimation of the background. It can be seen that the background is highly asymmetric which accounts for the asymmetry in the pixel maps. This is then subtracted from the pixel maps and the data interpolated to give the pixel maps shown in Figure 5(d).

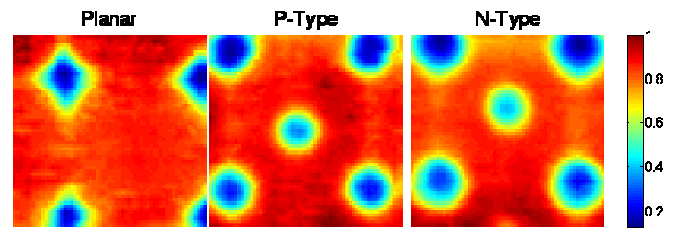


Fig. 6. $77.5\mu\text{m}$ square pixel maps, background subtracted, interpolated and normalised to the highest count.

The threshold while acquiring these maps was set at half the incoming photon energy. With the threshold set at this value we should see no double-counting or under-counting at the boundaries between two pixels. However, at the corners of the pixel there will be charge sharing between four pixels. Here it is likely that the energy in any single pixel will fall below threshold so we therefore see an area of low counts. In addition the area of low counts due to the central electrodes in the 3D detectors can be seen. Charge sharing at the pixel corners occurs to a lesser extent in the 3D, as will be shown in

Section D, and the dominating effect here is the electrode structure themselves.

C. Detection Efficiency

Due to the electrode structure of the 3D detectors columns ‘inactive’ areas exist in the pixel where the X-ray photon will not create a detectable charge cloud if it interacts. This will create non-uniform detection efficiency across the pixel as is clear from the pixel maps. In an effort to calculate the drop in efficiency at the central electrodes and corners we normalised the maps using the following method. A region on the pixel surface where we would expect 100% of interacting photons to be counted was chosen, as is illustrated by the area enclosed between the two circles in Figure 6(a). The mean of the top 5% of the values from this region was taken to be 100% efficient; this was done to account for statistical variation.

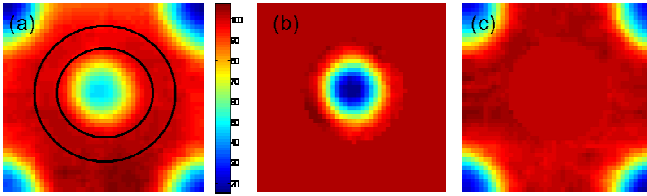


Fig. 7. Figures showing an example of the normalisation and detection efficiency measurement. (a) A pixel map, $55\mu\text{m}$ square, showing the ringed area which we assume has 100% detection efficiency, (b) Method used to calculate the drop in efficiency due to the central electrode and (c) the corners

To find the detection efficiency of the central electrode the area was isolated and the region around it filled with an area of 100% efficiency. This was compared to a pixel with 100% detection efficiency over the entire pixel area. The central electrode accounts for a drop in efficiency of 3% and 4% over the entire pixel in the N-type detector and the P-type detector respectively.

To find the detection efficiency at the corners of the 3D detectors the central electrode was isolated and the area filled with an area of 100% efficiency. This pixel and the planar pixel were compared to a pixel with 100% collection efficiency. A total loss of 7% in the detection efficiency was found for the four corners of the pixels for all three types of detector. Opposing effects were present at the corners of the pixel in the 3D detectors; a reduction in charge sharing and a drop in detection area cancel to give the similar detection efficiency as the planar device. The reduction in detection area is dominant as the circular regions of the electrodes are evident in the pixel maps. In the planar devices a diamond shape is evident at the corners of the pixels where only charge sharing occurs.

D. Charge-Sharing

Charge sharing occurs when charge clouds created by incident photons close to the pixel boundaries get collected by

two or more pixels. At low threshold levels this can lead to double counting and at high thresholds counts can be lost. Therefore the amount of double- and under-counting is an indication of the level of charge sharing present. Three different scans were performed on a corner area of a pixel on each of the three types of detector. These were performed using three different threshold settings. The low threshold scan used a threshold setting of *ca.* 25% of the incoming photon energy. The other scans were performed at threshold settings of *ca.* 50% and *ca.* 75% of the photon energy. The scans performed on the planar type detector are shown in Figure 8 (a-d).

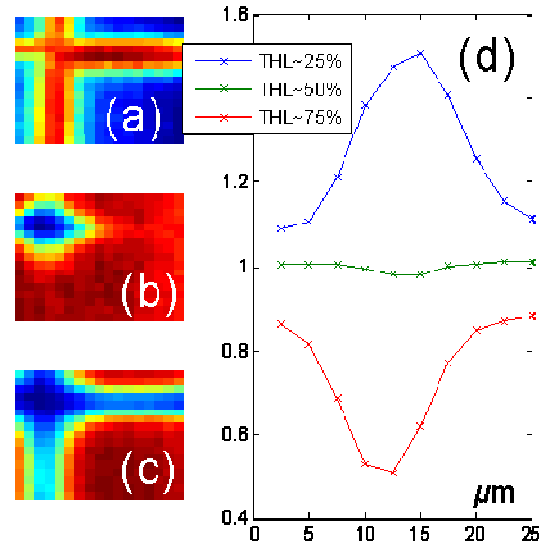


Fig. 8. Scans of a $42.5\mu\text{m}$ square region showing the top corner of a pixel in the planar device with threshold settings of (a) 25%, (b) 50%, and (c) 75% of the incident photon energy. (d) Normalised line sections showing the number of counts across the pixel boundaries between two neighbouring pixels.

The increase in counts at the pixel boundaries is plainly evident in the low threshold scan as is the drop in counts in the high threshold scan. The scan with a threshold at half the incoming photon energy, Figure 8 (b), shows a stable number of hits across the boundaries between two pixels. This is as expected as an incoming photon that shares more or less of half its incoming energy will be counted the neighbouring pixel or the incident pixel, respectively. A line section across this boundary should give a relatively stable number of counts as it passes from one pixel to its neighbour. The average of the number of counts is taken and the line section has been normalised to that value. A line section of the lower and higher threshold scans is taken and normalised with the mean value of the 50% threshold line, Figure 8 (d). It can be seen that at the edge of the pixels 50% of photons are double-counted at low threshold and lost at high threshold.

Comparing the planar results to the 3D device, Figure 9 (a-d), a significant reduction in double-counting and under-counting is seen. For the 3D device one in every three photons

is lost or double counted at the pixel edge. FWHM of the plots in Figure 8(d) and 9(d) show a reduction from $\sim 12\mu\text{m}$ to $\sim 8\mu\text{m}$, this indicates that charge sharing effects a much larger portion of the pixel in the planar device than that of the 3D device. A comparable improvement on the planar device is also seen in the P-type detector.

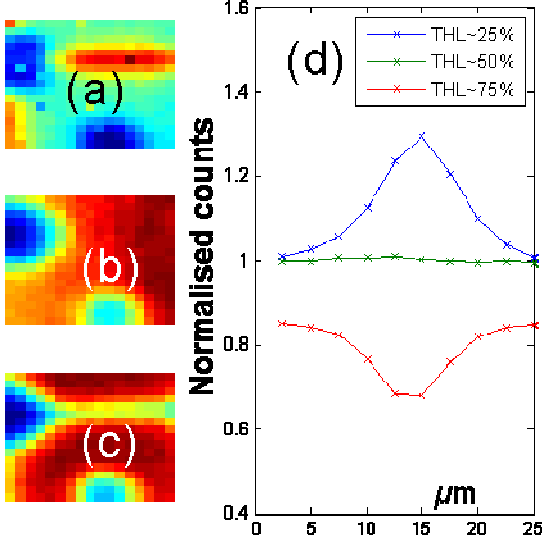


Fig. 9. Scans of a $42.5\mu\text{m}$ square region showing the top corner of a pixel in the 3D device with threshold settings of (a) 25%, (b) 50%, and (c) 75% of the incident photon energy. (d) Normalised line sections showing the number of counts across the pixel boundaries between two neighbouring pixels.

III. PION BEAM

A. Set-up

A pion beam provided by the Super Proton Synchrotron (SPS) was used to test a 3D N-type detector bump bonded to a Timepix chip. A telescope was built using six planar detectors with four of the chips bump bonded to Timepix chips and two bonded to Medipix chips. The telescope allowed the position of interaction of the individual pions on the device under test (DUT) to be measured. An accuracy of $<3\mu\text{m}$ was achieved. The angles of the telescope devices are adjusted to maximise charge sharing and thus minimise the extrapolation error of the beam onto the device under test, Figure 10. The 3D Timepix device was aligned perpendicular to the beam by using the cluster size distribution relative to the angle of rotation.



Fig. 10. The central device shown is the device under test. The six devices which make up the telescope are positioned either side.

B. Results

A measure of the detection efficiency is illustrated by the pixel map shown in Figure 11. This map was created by noting the position of a hit on the DUT. The hit pixel and its neighbours were examined and if a count was found a positive result was placed on the pixel map. The map therefore is a combination of the pixel responses of the entire matrix.

The pixel map was normalised using the same method as outlined in Section II(C). A higher efficiency than that of the map in Figure 7(a) can be seen. This is due to the threshold in this experiment being set just above the noise level. Here the loss of detection efficiency from the central electrode is 0.5% with an efficiency drop due to the corner electrodes of 5%.

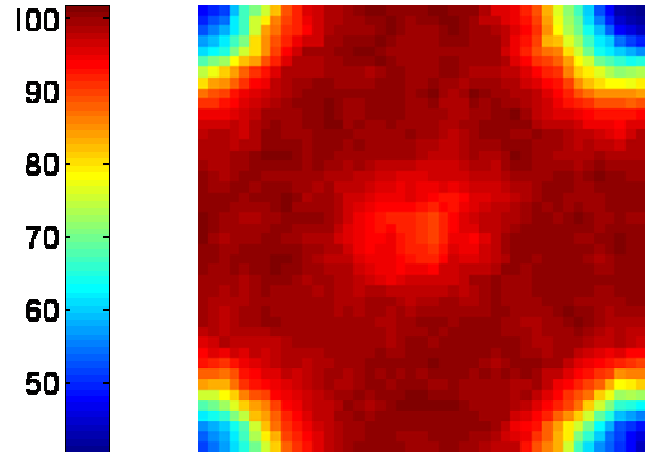


Fig. 11. $55\mu\text{m}$ square pixel map showing the detection efficiency for MIPs.

By using the TOT mode of the Timepix chip it was possible to view the energy deposited by each interacting particle. This information for each pixel was collected and used to produce the pixel map shown in Figure 12.

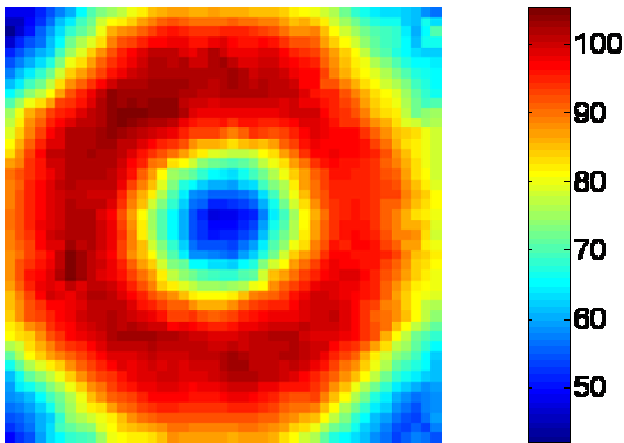


Fig. 12. 55 μ m square pixel map showing the detection efficiency for MIPs. The colour-bar shows the normalised ADC counts

A reduction in the charge deposited when a particle is incident on the electrodes is evident. This can be explained by the reduction of depleted Si in which the particle can interact. When the particle is incident on the electrode it has $\sim 35\mu\text{m}$ of depleted Si in which to create charge whereas in the surrounding region the full 285 μm thickness is available. Evidence of charge-sharing is seen in the drop of collected charge at the pixel boundaries.

IV. CONCLUSIONS

Novel 3D double-sided detectors have been fabricated, bump-bonded to Timepix and Medipix2 chips and tested with a synchrotron micro-focus X-ray beam. The non-uniform response of the pixels due to the electrode columns has been mapped. A drop in efficiency of 3 and 4% in the 3D N-type and P-type detectors respectively, was caused by the central pixel electrode. The corner electrodes show no deterioration to the pixel efficiency compared to the tested planar devices. Charge-sharing in the planar devices accounts for the same number of lost counts present in the 3D pixel due to the corner electrodes.

A significant reduction in charge sharing has been shown by the drop in double- and under-counting at the pixel boundaries. The drop in the area of the pixel affected by charge-sharing is indicated by the decrease in the FWHM of the line sections at the pixel boundary.

Detection maps using a MIP beam showing the non-uniformity were successfully created and complement the X-ray data. Here the threshold is lowered to just above the noise level and a drop of 0.5% efficiency is shown due to the central electrodes. Using TOT mode a pixel map of the energy deposited shows a significant drop in the energy deposited in the central and corner regions which correlate well with the electrode positions. However, the region of depleted Si under the electrode columns still provides sufficient signal for MIP

detection at the centre but when that charge is shared at the pixel corners, hits may fall below threshold and be lost.

ACKNOWLEDGMENT

This work has been partially supported by the Spanish Ministry of Education and Science through the GICSERV program "Access to ICTS integrated nano- and microelectronics cleanroom". This work was carried out in the context of the RD50 collaboration.

REFERENCES

- [1] J. Marchal, N. Tartoni, and C. Nave, "Synchrotron applications of pixel and strip detectors at Diamond Light Source," *Nuclear Instruments and Methods in Physics Research Section A: Accelerators, Spectrometers, Detectors and Associated Equipment*, vol. 604, pp. 123-126, 2009.
- [2] V. A. Wright, W. D. Davidson, J. J. Melone, V. O'Shea, K. M. Smith, L. Donohue, L. Lea, K. Robb, S. Nenonen, and H. Sipila, "Three-dimensional Medipix-a new generation of X-ray detectors," *Nuclear Science, IEEE Transactions on*, vol. 52, pp. 1873-1876, 2005.
- [3] G. Pellegrini, M. Lozano, M. Ullán, R. Bates, C. Fleta, and D. Pennicard, "First double-sided 3-D detectors fabricated at CNM-IMB," *Nuclear Instruments and Methods in Physics Research Section A: Accelerators, Spectrometers, Detectors and Associated Equipment*, vol. 592, pp. 38-43, 2008.
- [4] D. Pennicard, G. Pellegrini, M. Lozano, R. Bates, C. Parkes, and V. Wright, "Simulation Results from Double-Sided 3D Detectors," in *Nuclear Science Symposium Conference Record, 2006. IEEE, 2006*, pp. 1614-1618.
- [5] C. Fleta, D. Pennicard, R. Bates, V. O'Shea, C. Parkes, M. Lozano, G. Pellegrini, J. Marchal, and N. Tartoni, "X-ray detection with 3D Medipix2 devices," *Nuclear Instruments and Methods in Physics Research Section A: Accelerators, Spectrometers, Detectors and Associated Equipment*, vol. 607, pp. 89-91, 2009.
- [6] L. Tlustos, R. Ballabriga, M. Campbell, E. Heijne, K. Kincade, X. Llopart, and P. Stejskal, "Imaging properties of the Medipix2 system exploiting single and dual energy thresholds," in *Nuclear Science Symposium Conference Record, 2004 IEEE, 2004*, pp. 2155-2159 Vol. 4.
- [7] X. Llopart, R. Ballabriga, M. Campbell, L. Tlustos, and W. Wong, "Timepix, a 65k programmable pixel readout chip for arrival time, energy and/or photon counting measurements," *Nuclear Instruments and Methods in Physics Research Section A: Accelerators, Spectrometers, Detectors and Associated Equipment*, vol. 581, pp. 485-494, 2007.
- [8] Z. Vykydal, J. Jakubek, and S. Pospisil, "USB interface for Medipix2 pixel device enabling energy and position-sensitive detection of heavy charged particles," *Nuclear Instruments and Methods in Physics Research Section A: Accelerators, Spectrometers, Detectors and Associated Equipment*, vol. 563, pp. 112-115, 2006.